Electrochimica Acta 430 (2022) 141083

Contents lists available at ScienceDirect

Electrochimica Acta

journal homepage: www.journals.elsevier.com/electrochimica-acta

A novel hierarchically-porous diamondized polyacrylonitrile sponge-like electrodes for acetaminophen electrochemical detection

Mattia Pierpaoli [a,*], Pawel Jakóbczyk [a], Bartłomiej Dec [a], Chiara Giosuè [b], Natalia Czerwińska [b], Aneta Lewkowicz [c], Maria Letizia Ruello [b], Robert Bogdanowicz [a]

[a] Department of Metrology and Optoelectronics, Faculty of Electronics, Telecommunication, and Informatics, Gdańsk University of Technology, Gabriela Narutowicza 11/12, Gdańsk 80-233, Poland
[b] Department of Materials, Environmental Sciences and Urban Planning (SIMAU), Università Politecnica delle Marche, Via Brecce Bianche 12, Ancona 60131, Italy
[c] Institute of Experimental Physics of Gdańsk, University of Gdańsk, ul. Jana Bażyńskiego 8, Gdańsk 80-309, Poland

ARTICLE INFO

Keywords:
Carbon fibres
Graphene and other 2D-materials
Electro-chemical behaviour
Sensing
Chemical vapour deposition (CVD)

ABSTRACT

A novel composite electrode material consisting of tangled fibrous polyacrylonitrile-based hierarchically-structured nanocomposites has been produced by wet-spinning, carbonized and decorated with a carbon nano-architecture by microwave plasma-enhanced chemical vapor deposition and investigated as a metal-free electrode for the enhanced electrochemical detection of acetaminophen. Surprisingly, the hierarchical fiber architecture is the result of the synergistic action between surface etching, by the H_2 plasma, and nanostructure formation, by the C- and CH- radicals, which significantly affect the porosity and electrochemical performance. Moreover, by simultaneously conducting fiber carbonization and surface functionalization, it is possible to dramatically reduce the manufacturing time and to confer an 18-fold increase of the acetaminophen detection sensitivity, due to the sp^2-C defect-rich overgrown nanostructure, which represents a preferable site for the drug adsorption, as supported by the molecular dynamics simulation results. Because of the excellent performance, and the simple and scalable production method, the prepared composite is a promising candidate as a metal-free electrochemical sensor.

1. Introduction

Carbon functionalized nanofibers are effortlessly approachable and are characterized by a large surface area, as well as good electrical conductivity and chemical stability, which has made them desirable for many energy and environmental-related applications, for example as electrocatalysts, for energy storage, the detection of metals and biomolecules, and the adsorption of gases and water pollutants. Moreover, the ease of incorporating heteroatoms or nanostructures allows facile fiber functionalization and remarkable enhancement and tuning of the original properties.

Generally, the fabrication of polyacrylonitrile (PAN)-based carbon fiber involves three steps. Firstly, after the spinning process, the fiber must undergo stabilization. This step is usually conducted in air, at a low heating rate, and controlled temperature. Linear polymeric chains are converted into more complex and stable structures, through dehydration, cross-linking, cleavage of the nitrile triple bond, and transforming to C=N group by cyclization, which leads to the formation of the aromatic ladder structure. This whole process is critical to obtaining precursor fibers that are ready to withstand the high temperatures encountered during the next step [1]. Secondly, the carbonization process occurs in an inert atmosphere (such as N_2), in which all heteroatoms are removed as gases, which leads to the formation of haphazardly folded carbon sheets [2]. Thirdly, heat treatment up to 2500 K in inert gases improves the orientation of the basal planes and the stiffness of the fibers [3]. In order to increase the fiber-specific surface area, many authors have coated, grown, or decorated the surface of the spun PAN-fiber with complexes nanostructures. Nitrogen-doped carbon nanofibers were prepared by carbonizing electrospun polyacrylonitrile@polyaniline core-shell nanofibers, to obtain a rough surface, and decorated with CuO nanoparticles by a solvothermal method for the detection of glucose. The amperometric responses showed good selectivity to glucose in the presence of interfering species, such as ascorbic and uric acids [4]. In another work, CoMn-based zeolitic imidazolate framework nanosheets were grown over electrospun polyacrylonitrile fibers and used as an electrochemical sensor for the

* Corresponding author.
E-mail address: mattia.pierpaoli@pg.edu.pl (M. Pierpaoli).

https://doi.org/10.1016/j.electacta.2022.141083
Received 1 June 2022; Received in revised form 27 July 2022; Accepted 22 August 2022
Available online 26 August 2022

detection of α-synuclein oligomers. The derived aptasensor exhibited an ultralow detection limit of 0.87 fg mL^{-1} over a linear range of 1 fg mL^{-1} to 0.2 ng mL^{-1} [5]. Similarly, Yang and co-authors, synthesized carbon nanofibers decorated with Pt nanoparticles via electrospinning. The nanoparticles, characterized by a radius of ≈8.8 nm, were evenly dispersed in the fiber and they were formed during the PAN carbonization process, proving the possibility of simplifying the fiber production/functionalization method [6]. An improvement of the electrical conductivity, graphitization degree and sensitivity toward triglyceride detection, by embedding Ag nanoparticles, was also found by Mondal et al. [7]. While the fiber decoration with nanoparticles generally led to enhanced sensitivity, the synthesis process, together with the use of specific reagents, added complexity and raised the cost of the prepared composite. A few examples of the development of metal-free advanced sensing electrodes can be found in the literature [8]. Zheng et al. fabricated a carbon-only sensor based on a polyaniline-polyacrylonitrile-graphene composite for the determination of phenolic compounds in water [9]. Similarly, Ozoemena et al. encapsulated onion-like carbons into carbon nanofiber for the electrocatalytic detection of dopamine, reaching a limit of detection (LOD) of 1.23 μM [10].

The growth of diamonds on carbon fibers is a topic of current interest, due to their wide potential windows, and this has been investigated by a few authors. Micro and nanodiamond films were grown on carbon fibers by Almeida and coworkers by Hot Filament Chemical Vapor Deposition (HF-CVD) after seeding in a solution of nanodiamond powder [11]. On the other hand, two-dimensional carbon nanostructures, such as carbon nanowalls (CNWs) have attracted recent attention due to the high surface area and charge mobility, and fast electron transfer, making them perfect candidates as electrochemical sensors [12–14]. Li et al. grew CNW on electrospun PAN fibers by CVD without the assistance of any metallic catalysts and found that MPECVD-carbonized PAN fibers do not exhibit any significant change in the fiber diameter compared to furnace-carbonized ones [15]. Hsu et al. investigated the growth of CNWs on carbon nanotubes by a single process after stabilization and carbonization of the PAN fibers, finding a 10-fold increase of the specific surface area [16].

In our study, for the first time, a metal-free carbon-based fibrous electrode has been created by combining wet-spinning and CVD techniques, in order to overcome the transition from low-volume/high-cost to high-volume/low-cost composite development. We have proposed novel fabrication method based on carbon-on-carbon approach resulting in sustainable, disposable and facile electrodes optimized for electrochemistry. The polyacrylonitrile-based diamondized hierarchically-porous fibrous nanocomposites (HiDiPAN) were created in two steps: firstly, by simply controlling the solvent mass transfer during phase inversion in the wet-spinning phase, and secondly by tuning the gas phase composition within the CVD process. Fabricated HiDiPAN electrodes revealed high kinetics and electrochemical performance demonstrated here by acetaminophen and diclofenac detection, showing that the PAN fiber sponge-like surfaces reached one order of magnitude improvement in the LOD and 18-fold higher sensitivity.

2. Materials and methods

Polyacrylonitrile (PAN) with 150,000 molecular weight was purchased from Aldrich. Dimethylformamide (DMF, pure p.a.), potassium ferricyanide $K_3[Fe(CN)_6]$ and $K_4[Fe(CN)_6]\bullet 3H_2O$ were acquired from POCH (Poland). A stock phosphate solution (PS, 0.1 M) was obtained by mixing 8.7331 g of K_2HPO_4 and 125 μL of 85% H_3PO_4 in a 500 ml volumetric flask. All solutions were prepared with deionized water.

2.1. PAN fibrous sponge-like electrodes preparation

A schematic representation of the PAN fibrous sponge-like fabrication is displayed in Fig. 1. The hierarchical structure of PAN electrodes reveals maze-like pores looking similarly to the sponges. In that manner electrodes mimic multicellular organisms sponges having bodies filled with pores and channels permitting water to flow through them. In our case, the electrolyte penetrates those pores, thus the specific area of the samples is much larger than geometrical one.

PAN was dissolved in a concentration of 10%wt in DMF, under discontinuous stirring for 12 h at 60 °C, and left to rest for 24 h. Once a homogeneous solution was obtained, it was transferred to a syringe and spun through a water coagulation bath, using an in-house-made apparatus (schematic and documentation have been made available online). The syringe pump flow rate was set at 0.5 mL min^{-1}, using a 0.91 mm needle diameter. Then, the wet-spun PAN fibers were entangled and confined in a 15 × 10 mm aluminum mold and stabilized at 260 °C for 3 h, (heating rate 1 °C min^{-1}) to undergo cyclization, cross-linking, and dehydrogenation. The temperature was chosen based on the TGA results.

2.2. Porization and diamondization

While, in a conventional method, stabilized PAN may undergo carbonization in a furnace at a temperature up to 1700 °C in the presence of an inert atmosphere, in this study, to remove most of the non-carbon atoms, with a heating rate in the order of tens of degrees per minute, we performed carbonization and the subsequent surface functionalization directly in the MPECVD chamber (Seki Technotron, 2.45 GHz, 1.5 kW). The sample holder was heated to 650 °C, and a 20 min-long hydrogen plasma treatment was used to partially etch the amorphous carbon. In the case of the H_2 sample, the plasma treatment was protracted for the whole duration of the process. For all of the other samples, a different gas mixture of H_2, CH_4 and B_2H_6 was used to grow the nanostructure to functionalize the fiber surface, with a total pressure of 40 Torr and microwave power of 1100 W. The role of diborane gas

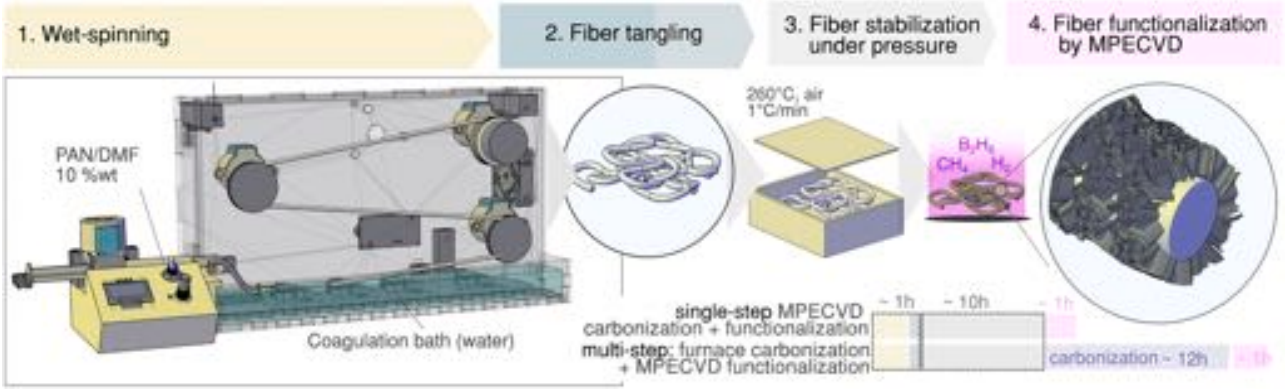

Fig. 1. Schematic of PAN fiber composite fabrication.

was to enhance the re-nucleation and twinning surface process of the CVD-grown graphene stacks. While in our previous study, we reported the importance of N_2, together with the other gases to improve the CNW growth [13], in this study, the stabilized PAN fiber contains nitrogen which is eliminated during the carbonization process.

2.3. Electrode morphological characterization techniques

Scanning electron microscopy (SEM) was performed by a Phenom XL using a 15 kV beam accelerating voltage, working in low vacuum mode. Raman scattering was measured upon excitation by a HeNe 633 nm laser; the spectral resolution was equal to 2 cm^{-1} in the range of 200–3500 cm^{-1} with an integration time of 5 s (20 averages); the diffraction grating had 300 lines mm^{-2}. Three spectra were acquired for each sample in different spots. The baseline was subtracted, and the data was normalized and fitted. Thermogravimetric analysis (TGA, Mettler Toledo TGA/SDTA 851) was performed on the wet-spun PAN (in air, 25–250 °C, 2 °C min^{-1}) and after stabilization (in N_2, 25–1000 °C, 10 °C min^{-1}).

2.4. Electrode electrochemical characterization setups

The electrochemical performance of the carbon sponge electrodes was investigated by cyclic voltammetry (CV) and electrochemical impedance spectroscopy (EIS) using a VMP-300 BioLogic galvanostat-potentiostat (France) under the EC-lab software. All electrochemical investigations were carried out in a three-electrode cell system after bubbling the solution with argon. The carbon sponge electrode, a platinum wire and an Ag/AgCl/3 M KCl electrode were used as the working electrode (WE), auxiliary electrode (AE), and reference electrode (RE), respectively. The mass of the working electrode (WE) was from 15.5 mg to 22 mg. The electrochemical measurements were recorded in 1 mM Fe $[(CN)_6]^{3-/4-}$ (1:1) with 0.05 mol dm^{-3} of phosphate solution (PS) as supporting electrolyte. The scan rate applied for cyclic voltammetry (CV) was equal to 100 mVs^{-1}. Differential pulse voltammograms were obtained under the following conditions: the potential ranging from 0 to 0.8 V (vs. Ag/AgCl/3.0 M KCl), a 100 ms pulse width, a 50 mV pulse height, a step time of 500 ms, and a scan rate of 16 mV s^{-1}. The EIS were recorded at open circuit potential across the frequency from 0.01 Hz to 100 kHz. The peak-to-peak amplitude was equal to 10 mV. Specificity, reproducibility, and stability of the carbon sponge electrodes were calculated [17].

2.5. Molecular dynamics simulation

The molecular dynamics simulations (MDS) were perfomed in QuantumATK software from Synopsys using the TremoloX engine. The Reactive Force Field (ReaxFF) method was utilized, with force field description in accordance with work of Liu et al. [18]. The simulation was firstly subjected to geometry optimization using Limited Memory Broyden–Fletcher–Goldfarb–Shanno algorithm [19]. The modeled system was optimized below 0.05 eV/Å for Force tolerance, and 0.1 GPa for Stress error tolerance. Molecular dynamics simulations were done with 1fs step, and for 50ps, using Berendsen thermostat [20]. The reservoir temperature was set to 300 °K.

3. Results and discussion

3.1. Electrode characterization

3.1.1. Morphological and molecular characterization

Fig. 2a reports a SEM image of the stabilized PAN fiber. After immersion of the polymeric solution in the coagulation bath, the mass transfer between the solvent and nonsolvent is responsible for polymer precipitation and fiber formation. Due to the instantaneous demixing, a finely porous layer is formed on the surface (Fig. 2a, inset) and a tree-

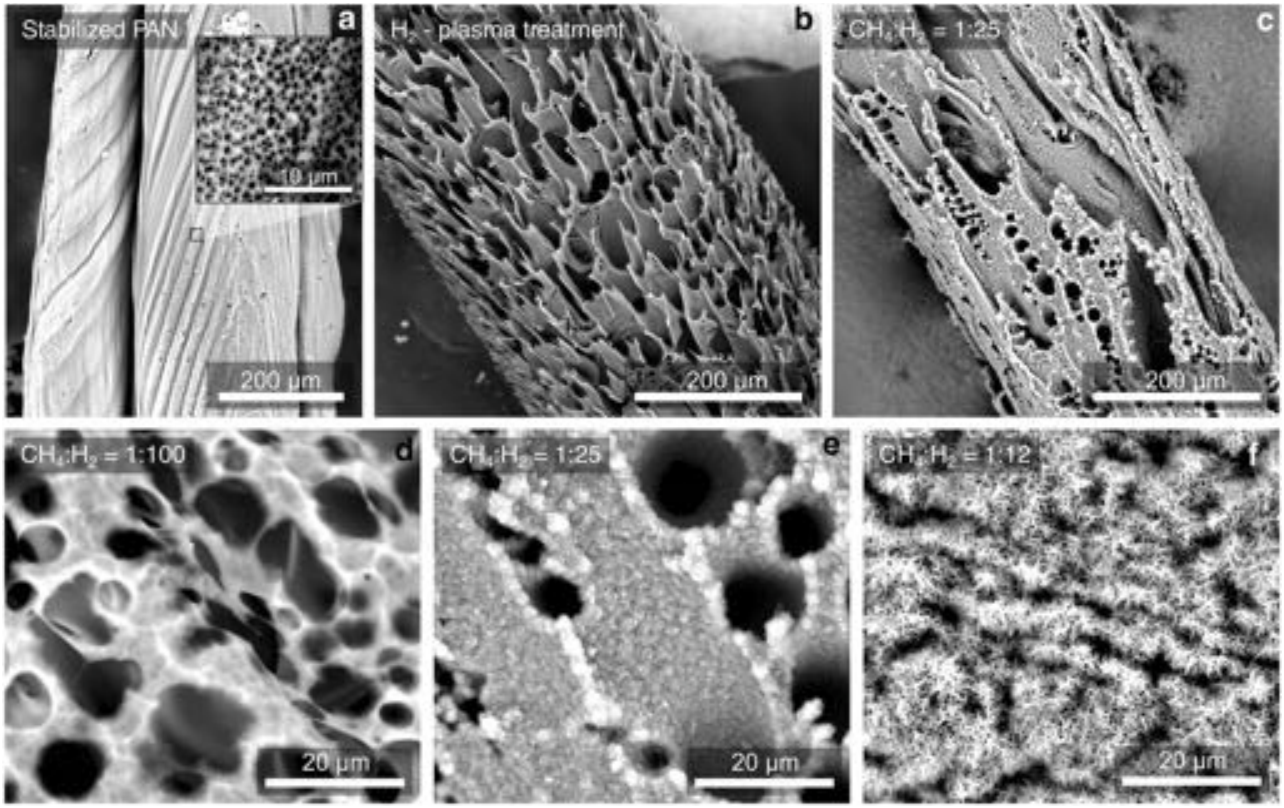

Fig. 2. (a) Stabilized PAN fiber; (insert) magnification of the fiber surface porosity. (b) PAN fiber subjected to a 20 min H_2 plasma, (c) PAN fiber covered by CVD with hybrid carbon nanostructures. Micrographs of the PAN hybrid composites obtained by CVD using (d) 1:100, (e) 1:25, and (f) 1:12 CH_4:H_2 gas mixing ratios.

like macrovoid structure in the fiber bulk (Figs. S1, S2).

The temperature at which the stabilization was performed was chosen based on the TGA analysis. In particular, from Fig. S3 it is possible to observe that no oxidation occurs before 240 °C, with a total mass loss equal to 1.8%, which is attributed to the loss of adsorbed water. The same sample was then heated up to 1000 °C in N_2 and the TGA and DTG curves were recorded (Fig. S4). Here, the carbonization took place, which includes a two-step degradation process. A large exothermic peak was found at 308 °C (starting at 303 °C), corresponding to a 25.6% mass loss which was probably due to the cyclization of the nitrile groups and the C-C dissociation in the main chain [21,22]. At the end of this step, a further step of weight loss occurs in nitrogen, starting at around 520 °C, confirming the dissociation of the C-C bond [23]. After 900 °C, 17% of the initial mass is left. Experimentally, it is possible to observe the fiber thinning and shrinking after the heat-treatment process.

During the CVD deposition, fiber etching and carbon nucleation occur simultaneously. The H_2 plasma is mainly responsible for the fiber etching of the outer surface, resulting in the exposure of the inner fiber structure (Fig. 2b). The presence of hierarchically organized cavities is due to the solvent diffusion away from the fiber in the coagulation bath. The subsequent introduction of CH_4 into the reactor and formation of C- and CH- radicals that, by limiting the H_2-induced etching, favor the growth of different carbon nanostructures. Fig. 2c reports the formation of an outer diamond-like shell around the fiber. Indeed, by varying the CH_4:H_2 gas ratio, it is possible to tune the nanostructure morphology [13], ranging from BDD-like (HiDiPAN-1:100, Fig. 2d) to CNW-like (HiDiPAN-1:12, Fig. 2f), through its intermediate (HiDiPAN-1:25 Fig. 2e). In particular, it is possible to appreciate two different aspects: firstly, how the excess of C- and CH- produces a more uniform coating of the fiber, limiting the outer fiber etching and, secondly, the introduction of a maze-like porosity due to the formation of carbon nanowalls.

The Raman spectra displayed in Fig. 3 revealed the characteristic G and D bands at (1573 ± 11) cm^{-1} and (1325 ± 5) cm^{-1}, respectively. In particular, it could be noticed that these peaks are much sharper with increasing CH_4 content in the gas mixture and that the relative intensity ratio of the D peak to the G peak – I(D)/I(G) – varies accordingly.

Raman spectrum decomposition was performed taking into consideration the five Raman peaks in the 1200–1700 cm^{-1} spectral range and the three in the 2200–3200 cm^{-1} interval (Fig. 3, insert). The G band (generally reported at ≈1580 cm^{-1}) is related to an ideal graphene lattice since it is associated with the doubly degenerate and in-plane transverse phonon mode. It is known that the position of the G peak and its FWHM are sensitive to doping, defects and strain, which increase with increasing disorder due to the quantum confinement effect [24]. Thus, in our study, it is possible to observe an apparent decrease of the defects (Fig. 4a) with the increasing CH_4:H_2 gas feed ratio during the

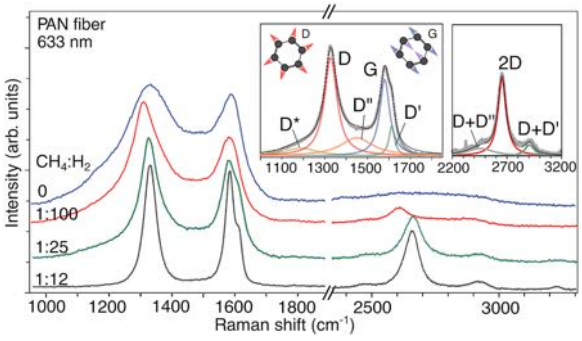

Fig. 3. Raman modes observed in the differently prepared PAN-based composites in the spectral region from 1000 to 3250 cm^{-1} excited at 632.8 nm. The decomposition of the Raman spectra of sample 1:25 into 5 components (G, D, D', D'' and D*) for the 1200–1700 cm^{-1} range and into 3 features (2D, D+D", D+D') for the 220–3200 cm^{-1} range, using Lorentzian fitting.

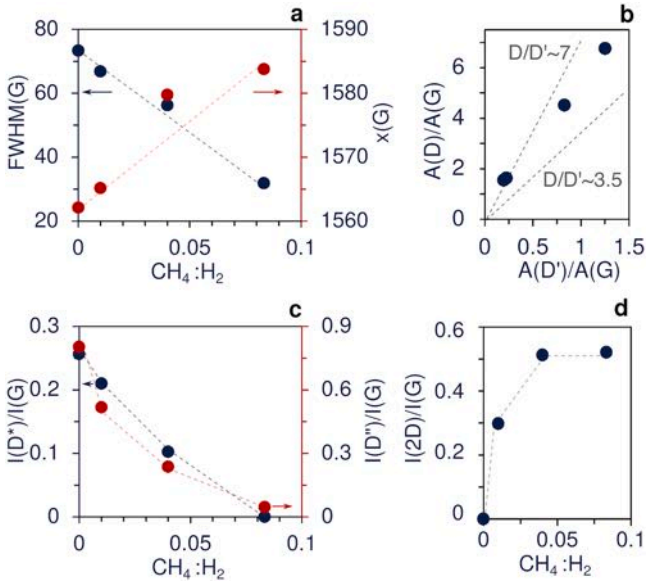

Fig. 4. Results of the Raman spectra fitting. (a) FWHM and peak position of the G band, as a function of the CH_4:H_2 ratio. (b) I(D)/I(G) as a function of the I(D)/I(G) ratio. (c) I(2D)/I(G) ratio as a function of the CH_4:H_2 ratio.

CVD process. This aspect can be explained by the faster formation of a new sp^2-rich carbon layer on the composite surface, due to the higher concentration of CH radicals. The A(D)/A(G) varies widely from 1.5 to 6.7, exhibiting a monotonous evolution when moving from the highest to the lowest CH_4:H_2 ratios (Fig. 4b).

The D' peak (≈1605 cm^{-1}) is noticeable as a shoulder peak of the G peak, and it has been reported in the literature that the I(D)/I(D') ratio can be usefully used to identify the nature of the defects. Indeed, with an average I(D)/I(D') ratio of ~6.5, it is possible to suppose that vacancy-type defects are predominant, or it may be due to the presence of nitrogen-dopants [25] originating from the PAN fiber. Interestingly, it has been reported that the 2D band (≈2630 cm^{-1}) decreases in intensity with the increasing defect density [26], and in the current study, it emerges with the increasing CH_4 content, and it is absent for the H_2-treated PAN fiber, since the substrate can be considered amorphous (Fig. 4d), and it reaches a plateau for a CH_4:H_2 ratio greater than 0.04. Similarly, the disappearance of the D* band (≈1190 cm^{-1}), ahead of the D peak, with increasing CH_4 content, suggests the elimination of oxygen-containing groups [27], since its presence has been related to a disordered graphitic lattice in soot samples, provided by the existence of sp^3 bonds [28]. Moreover, the absence of the 2D peak in the only-H_2--treated sample also supports the hypothesis of the presence of oxygenated functional groups together with the abundance of amorphous carbon, related to the carbonized PAN fiber itself. The appearance of the 2D band with the introduction of CH_4 in the gas mixture and the shift of its maxima position indicates an increase of the sp^2-C content [29]. The characteristic diamond peak positioned at 1332 cm^{-1} was not clearly observed due to the strong Raman signal generated by sp^2-C, especially for the employed wavelength. Nevertheless, analogous nanostructures were previously studied at silicon wafers revealing diamond exciton sharp peak at 289.0 eV, the other specific feature of a dip at 302.5 eV in EELS and characteristic diamond-phase ascribed SAED patterns [30,31].

3.1.2. *Electrochemical performance*

The surface character and electron transfer behavior of the fabricated electrodes were investigated by electrochemical cyclic voltammetry (CV) and electrochemical impedance spectroscopy (EIS).

The CV measurements were conducted at different scan rates (5, 10, 20, 50, 100, 150, 200, 300, 400 $mV \cdot s^{-1}$). The characterization of electrochemical processes in terms of the rate-limiting step (diffusion or

adsorption) at surface of the PAN-based composite electrodes were carried out. For electrochemically reversible electron transfer processes involving freely diffusing redox species, the Randles-Sevcik Equation describe the dependence of the peak current on scan rate and reveals that plots of current versus square root of scan rate should be linear [32, 33]. Fig. 5 shows anodic and cathodic currents of the faradaic process increase linearly with square root of scan rate which is consistent with diffusion limitation of redox processes. Also peak to peak separation for low scan rate (5 mV s^{-1}) is not equal to zero and is close to 57 ± 2 mV, 69 ± 4 mV, 57 ± 2 mV and 47 ± 3 mV for HiDiPAN-1:12, HiDiPAN-1:25, HiDiPAN-1:100, H_2-treated composite electrodes respectively, which proves the occurring single-electrode redox processes limited by diffusion.

Fig. 6a shows a comparison of the CV curves for the different electrodes in a solution of 1 mM $K_3[Fe(CN)_6]/K_4[Fe(CN)_6]$ in the weight ratio 1:1, in 0.05 M PS water solution at a scan rate of 100 mVs^{-1}.

Well-defined redox peaks were observed at 0.289 V (HiDiPAN-1:12 electrode), 0.407 V (HiDiPAN-1:25 electrode), and 0.455 V (HiDiPAN-1:100 electrode). Much less pronounced peaks were seen for the hydrogen-treated PAN-based samples on which no surface decoration occurred. This demonstrates non-uniform surface and complex reactions with different kinetics occurring on the fiber surface. The peak-to-peak separations (ΔEp) are 92 ± 5 mV, 351 ± 15 mV, 252 ± 11 mV, 145 ± 12 mV for the HiDiPAN-1:12, HiDiPAN-1:25, HiDiPAN-1:100 and H_2-treated composite electrodes, respectively. As shown in Fig. 6a, a pair of redox peaks with an ΔEp of 92 mV was observed at the HiDiPAN-1:12 electrode, whereas at the HiDiPAN-1:25 and HiDiPAN-1:100 electrodes, the ΔEp increased to 407 mV and 455 mV, respectively, with decreasing sp^2-C content. The lower peak-to-peak separation for the HiDiPAN-1:12 electrode suggests faster electron-transfer kinetics as compared to the HiDiPAN-1:25 and HiDiPAN-1:100 electrodes. This is due to the easier adsorption of electroactive ions by the sp^2 carbon [34]. The higher peak current magnitudes values for the 1:25 composite electrode could be related to its characteristic morphology: differently to the 1:12 composite, the micropores are still evident and they are easily accessible by the electrolyte, however, it possesses a higher surface area and lower electrode material resistance compared to the 1:100 sample. EIS can provide a more detailed study of the processes that occur at the electrode/electrolyte interfaces. The interface can be modeled by an equivalent circuit, which includes the ohmic resistance of the electrolyte (R_s), the Warburg impedance (Z_w), the charge-transfer resistance (R_{ct}), and electrochemical double-layer capacitance (C_{dl}) [35]. Fig. 6b presents the Nyquist plots obtained for the carbon composite electrodes, which were fitted based on the equivalent circuit (Fig. 6b, inset) using the EIS Spectrum Analyser software. The resulting Nyquist diagram includes a semicircular part and a linear part. The semicircular part at higher frequencies corresponds to the charge-transfer resistance (R_{ct}) and the resistance of the pores (R_p). Two time constants are shown in the Bode plot (Fig. 6c). The linear part (Fig. 6d) at lower frequencies is related to the diffusion process. Therefore the equivalent circuit includes the ohmic resistance of the electrolyte (R_s) in series with two-time constants (R and C in parallel), including pore resistance and constant phase element in-place capacitance because of the heterogeneous character of the material (R_p, CPE_p) and the charge transfer process between the electrolyte/electrode interphase and the constant phase element (R_{ct}, CPE_{dl}), and the Warburg element [35]. Table 1 displays the

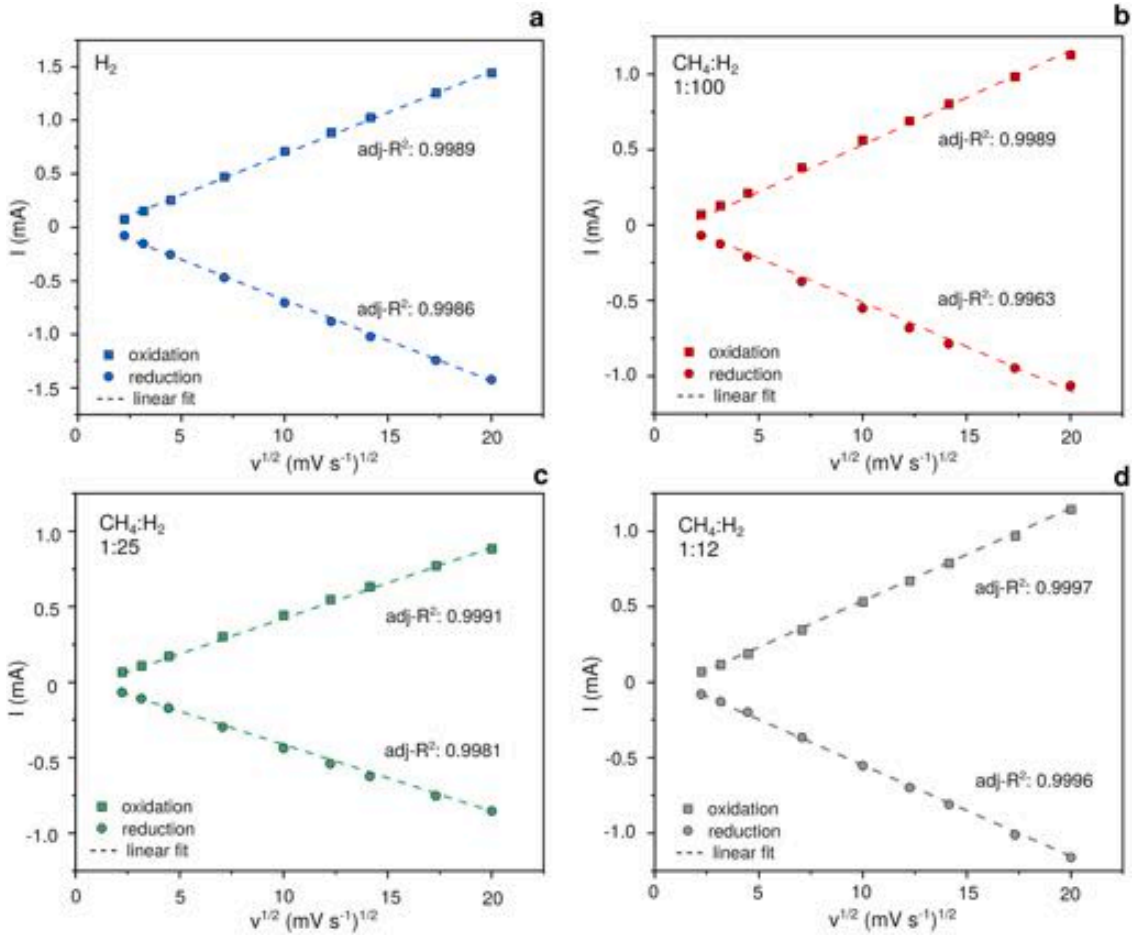

Fig. 5. Cyclic voltammetry of (a) H_2, (b) CH_4:H_2 1:100, (c) CH_4:H_2 1:25, (d) CH_4:H_2 1:12, PAN-based composite electrodes immersed in 1 mM $[Fe(CN)_6]^{3-/4-}$ in 0.1M PBS as a function of scan rates.

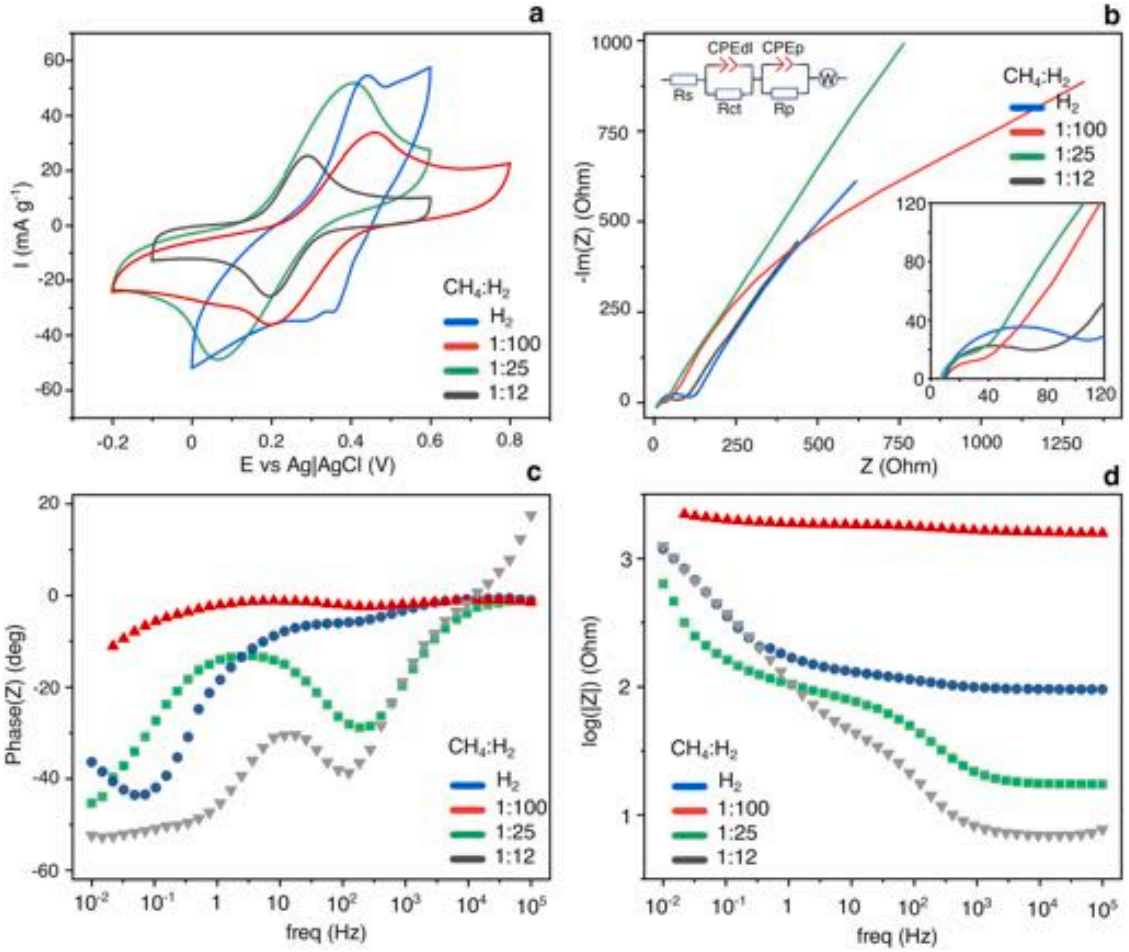

Fig. 6. (a) Cyclic voltammograms and (b–d) – Impedance spectra of PAN-based composite electrodes measured in a 0.05 M PS with 1 mM $K_3[Fe(CN)_6]/K_4[Fe(CN)_6]$ in a weight ratio of 1:1, vs. Ag/AgCl in 3 M KCl.

Table 1
Summary of electrochemical parameters obtained by CV (Ia, Ic, ΔEp, Ea, at 100 mV s^{-1}) and EIS (R_{ct}, R_p, at open circuit voltage) of all PAN-based composite electrodes in a 0.05 M PS solution with 1 mM $K_3[Fe(CN)_6]/K_4[Fe(CN)_6]$ in a weight ratio of 1:1, vs. Ag/AgCl in 3M KCl.

Material	I_a (mA)	I_c (mA)	ΔE_p (mV)	E_a (mV)	E_c (mV)	R_{ct} (Ohm)	R_p (Ohm)
PAN/H_2	54.7 ± 8	-34.8 ± 3	145 ± 12	439 ± 32	294 ± 16	18 ± 0.7	5 ± 0.3
HiDiPAN-1:100	34.2 ± 3	-36.3 ± 3	252 ± 11	455 ± 11	203 ± 14	166 ± 9	80 ± 7
HiDiPAN-1:25	52.3 ± 4	-48.6 ± 3	351 ± 15	407 ± 18	66 ± 11	23 ± 3	34 ± 2
HiDiPAN-1:12	25.6 ± 2	-26.0 ± 1	92 ± 5	289 ± 13	197 ± 12	37 ± 7	21 ± 2

electrochemical parameters obtained by fitting of EIS. The HiDiPAN-1:25 and the HiDiPAN-1:12 are characterized by a lower R_{ct} compared to the HiDiPAN-1:100.

The lowest R_{ct} of the hydrogen-treated PAN fiber is due to the significant structural disorder, rich in defects which are beneficial for accelerating electron transfer between the electrode and species in solution. However, the disadvantage of this material is the higher anode current than the cathode current, which indicates irreversible reactions taking place on the surface of the material (Fig. 6a). It can also be seen that the CVD-grown layer on the surface of the carbon material increases the pore resistance R_p together with the development of a more complex porosity (Table 1). In addition, the Bode plots illustrate the complementary EIS data, in which the smallest impedance modulus at high frequencies is presented by the 1:12 composite electrode and at low frequencies for the 1:25 composite electrode, as shown in Fig. 3c. It shows the lowest phase angle for the HiDiPAN-1:12, i.e., -53°, while for the HiDiPAN-1:100 electrode this value is at about -10°, as shown in Fig. 3(c), so a more capacitive behavior is recorded for the HiDiPAN-1:12 composite electrode.

3.2. Acetaminophen detection

The HiDiPAN electrodes were applied to detect acetaminophen in a 0.1 M PS. The differential pulse voltammetry (DPV) technique was employed to characterize the electrodes due to its excellent background suppression and higher sensitivity than the cyclic voltammetry (CV) technique. The HiDiPAN-1:12 is considered as optimal for acetaminophen determination in this work. In Fig. 7 was observed one well-separated peak at 0.38 V in the concentration range from 6 to 150 μM.

At the same acetaminophen concentration, the oxidization peak current measured by the PAN treated only by H_2 plasma is lower than the CVD-grown electrodes and possesses higher background currents. This may be due to the lower active surface area of the electrode material compared to the PAN composites containing nanowalls [36,37]. The current response of acetaminophen oxidation during DPV increases with the amount of carbon sp^2 in the sponge electrode structure (HiDiPAN-1:100 < HiDiPAN-1:25 < HiDiPAN-1:12). This is due to the easier adsorption to the sp^2 carbon structure and thus detection. Fig. 8a–d show the calibration curves for the HiDiPAN composite electrodes. From the slopes of linear calibration curves, the sensitivities were calculated.

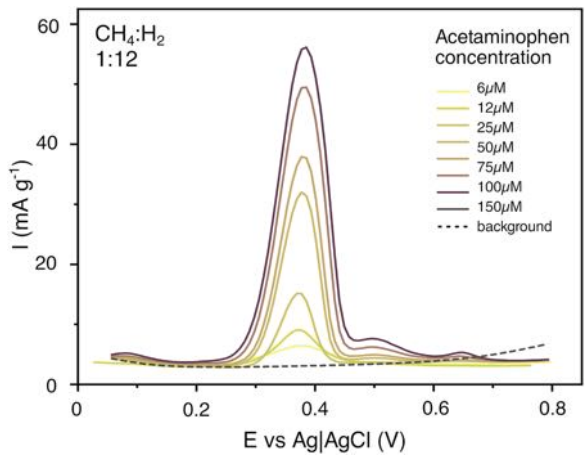

Fig. 7. (a) DPV determination of acetaminophen at PAN-composite (CH_4:H_2 1:12) electrode in mixtures containing acetaminophen in the concentration range from 6 to 150 μM in PS, 0.1 M.

It can be seen that the electrode with the highest amount of sp^2 carbon (CNW), i.e. the 1:12 composite electrode, has the best sensitivity (the highest slope of the calibration curve) [37]. The high sensitivity of the electrode can be attributed to the fact that acetaminophen easily adsorbs on the p-electron-rich graphene surface via π-π interactions [38, 39]. In particular, the benzene ring of acetaminophen and the one-dimensional planar carbon structure can also accumulate acetaminophen molecules and thus enhance the detection performance, as an adsorption-controlled process [40]. For the HiDiPAN-1:12 composite, two linear behaviors can be seen, ranging from 6 to 100 μM and between 100 and 250 μM, while for the HiDiPAN-1:25 and HiDiPAN-1:100, the calibration curves exhibit two different response areas depending on the acetaminophen concentration. This phenomenon may be related to the participation of different materials in the structure of the electrode, which influences various phenomena taking place on the electrode (e.g. minor or greater impact of adsorption and diffusion) [41]. The lower the CH_4:H_2 ratio in the composite synthesis process, the greater the acetaminophen detection range, but the lower the sensitivity of the electrode (Fig. 8a–d). In the case of the H_2-treated PAN-based electrode, in the absence of an overgrown carbon nanostructure, only one linear range is present. In the case of HiDiPAN-1:100, this is in the range of 25–250 μM, but with an order of magnitude lower sensitivity than the HiDiPAN-1:12 electrode. The sensitivity decreases with the decreasing CH_4 feed. The weakest sensitivity is that of the H_2 plasma-treated electrode.

The limit of detection (LOD) was calculated by the method that uses the equations containing the standard deviation (σ) of the estimated quantity (net signal) where s is the slope of the calibration curve [42]: LOD = 3.3 σ/s. The limits of detection were equal to 19 μM, 42 μM, 98 μM and 159 μM of acetaminophen for composites fabricated in CH_4:H_2 ratios 1:12, 1:25; 1:100 and pure H_2, respectively. A possible explanation for the better performance of the nanowall-decorated electrode may not only be the increased specific surface area, but also the change of the acetaminophen oxidation mechanism, by shifting from a one-proton and two-electron to a two-proton and two-electron process [34].

In order to correlate the electrochemical with the Raman results, it is worth highlighting the dual function of CVD plasma, governed by H_2-plasma etching and CH-radical nanostructure formation. In presence of

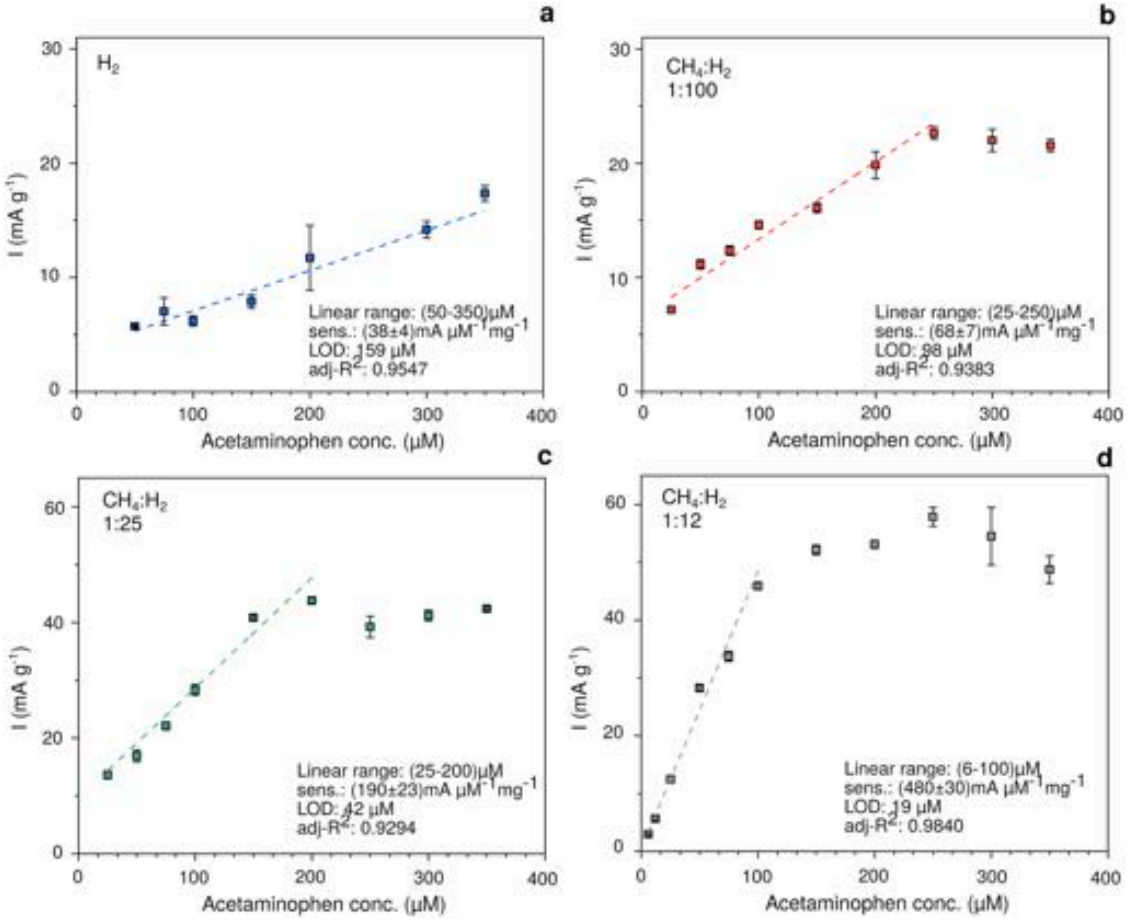

Fig. 8. Calibration curves corresponding to the acetaminophen analysis by (a) H_2, (b) CH_4:H_2 1:100, (c) CH_4:H_2 1:25, (d) CH_4:H_2 1:12, PAN-based composite electrodes.

H_2-plasma only, the outer amorphous carbon is etched, exposing the PAN turbostratic structure, rich in the edge-terrace surface, while, with the CH_4 introduction, the crystallite grows in size, resulting in basal-plane rich surface (HiDiPAN-1:100). With increasing CH_4 concentration, the formation of a microsized-roughness, led to the increase of the surface area, with also the formation of edge terraces (HiDiPAN-1:25), becoming then predominant and rich in edge planes (HiDiPAN-1:12), due to the peculiar maze-like graphene stacks formation (Fig. 9a). This aspect is shown in Fig. 9b, by the A(D)/A(D') ratio. It is recognized that the D and D' peak intensities increase with the increasing amount of defects. The D′ transition has been observed in graphene with defects caused by inductively coupled plasma [43], Ar ion bombardment [44], and in defective graphite during compression/decompression cycles [45]. Its origin has been related to graphene layers that have a graphite layer only on one side [46] and it has been assigned to the lattice vibration analogous to that of the G band. To differentiate between different defect types, the relative peak intensity, expressed as the ratio of the integrated area of the D and D′ bands, has been preferred because the area under the band represents the probability of the whole scattering process [43–45]. The ratio has been found to grow from 5.5 to 7.9 with increasing CH_4 content. The electrochemical activity of the basal plane and edge plane of graphite substantially differs: due to the prominent presence of edges terraces and planes in the HiDiPAN-0 and HiDiPAN-1:12 samples, the R_p is lower and the heterogeneous electron transfer is faster (Fig. 9b), which is in agreement with the findings of Velický et al. [47]. It has been reported that the introduction of defects to carbon nanomaterials may result in an improvement of the sensing performance [39,48]. It is known that the FWHM(G) always increases with the increasing disorder because this parameter is sensitive to all types of defects, either in the sp^2 rings or chains, and it is inversely dependent on the crystallite size (for $2 < La < 10$ nm) [46]. For these reasons, in our study, the edge-rich composites, characterized by a low degree of disorder and large crystallite size possess a lower acetaminophen LOD and higher sensitivity.

3.3. Stability, specificity and reproducibility, of the hierarchically-porous sponge electrodes

To evaluate the stability of the HiDiPAN electrodes, DPV was performed at various time interval since its immersion in the analyte solution. Results are reported in Table 2. The current response of acetaminophen for 75 μM concentration showed changes from 2.1% for HiDiPAN-1:12 till 5.3% for H_2- treated PAN composite. An RSD lower than 5% has been found for the composites subjected to CVD-growth.

Sensor reproducibility has been evaluated by performing detection experiments using the synthesized PAN-based composite electrodes in different time periods. A signal reproducibility of 90% was achieved.

A crucial challenge in applicability of sensors is their ability to sense analytes in the presence of other coexisting compounds. For examining the discrimination ability of the PAN-based composite materials, the current responses of diclofenac and acetaminophen were compared in the presence of different compounds in wastewater (Figs. 10, and S6).

Moreover, it can also be seen that the higher amount of BCNW in the structure of sensor material, the lower the oxidation potential of the analytes is recorded. Calibration curves were also made for the detection of diclofenac (Fig. S7), which allows to conclude that the material can also be used to detect of diclofenac.

Table 2
The stability evaluated using: H_2, CH_4:H_2 (1:100), CH_4:H_2 (1:25), CH_4:H_2 (1:12), PAN-based composite electrodes.

Electrode material	Current response (μA)			RSD (%)
	10 min	20 min	30 min	
PAN/H_2	111.7	124	116	5.3
HiDiPAN-1:100	200	208	214	3.4
HiDiPAN-1:25	421	439	399	4.8
HiDiPAN-1:12	617.6	635	644	2.1

3.4. Molecular dynamics simulation

Molecular dynamics simulation was performed to investigate how the acetaminophen is preferably adsorbed on the surface of the electrode. Modeled systems were calculated starting from three basic configurations, in which acetaminophen is found on the side of a HiDiPAN-1:12 nanowall-like structure, with oxygen termination (Fig. 11a), on top with oxygen termination (Fig. 11d), and top with hydrogen termination (Fig. 11g). MDS results showed that the most energetically favorable configuration is the one where acetaminophen is on top of the oxygen-terminated nanostructure (Fig. 11d, f). In particular, in this configuration, are observed hydrogen bonds and the mean distance between molecule and nanostructure is shortest, equal to 2.80 Å, with an adsorption energy of -33 kcal/mol. The second most favorable configuration is the one with acetaminophen on the side of the nanostructure, with O-termination (Fig. 11a–c). The adsorption energy was estimated equal to -12.94 kcal/mol and the mean distance between surface and molecule is 3.25 Å. Moreover, the above-mentioned configuration is the least stable and acetaminophen slides down the wall-like nanostructure. Interestingly, it was also found that the length of the vertical carbon wall is not influencing acetaminophen behavior, including the sliding behavior on side of structure.

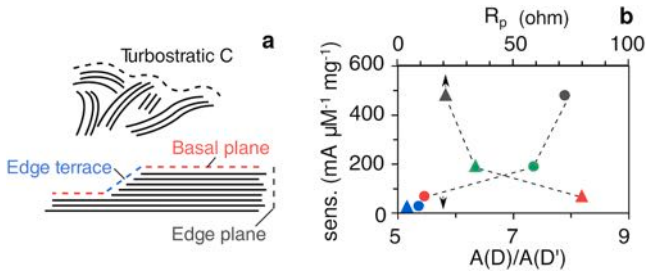

Fig. 9. (a) Schematic of the different surfaces occurring in the different composites. (b) Correlation between the defect type, as described by the A(D)/A(D') ratio, R_p, and acetaminophen sensitivity.

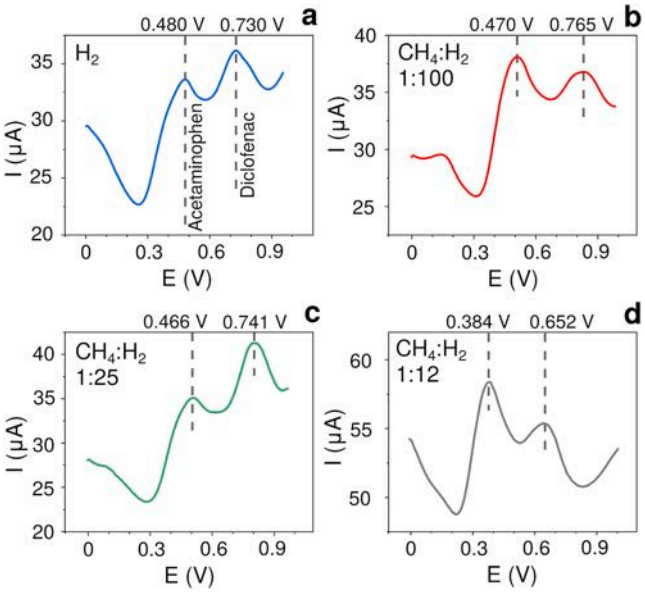

Fig. 10. Differential pulse voltammetry curves of acetaminophen and diclofenac in wastewater recorded using: (a) H_2, (b) CH_4:H_2 1:100, (c) CH_4:H_2 1:25, (d) CH_4:H_2 1:12, PAN-based composite electrodes.

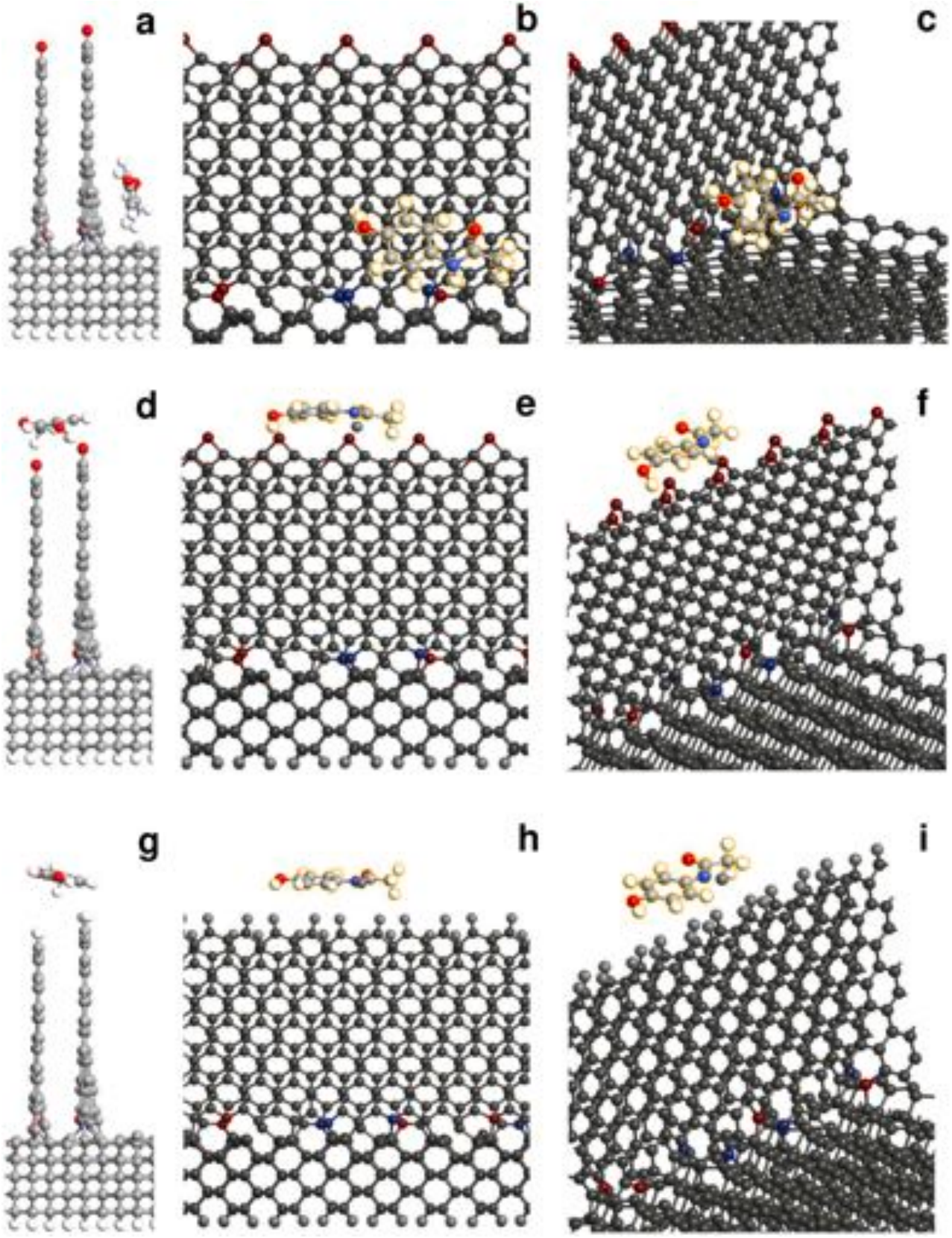

Fig. 11. Final MD step of NWs with acetaminophen: (a–c) acetaminophen on side of CNW, (d–f) acetaminophen on top with oxygen termination, (g–i) acetaminophen on top with hydrogen termination.

In the last configuration (Fig. 11g–i), where acetaminophen is on the top of the hydrogen-terminated nanostructure, the adsorption energy is equal to + 36.64 kcal/mol, meaning that the molecule is repelled from the top edges of the graphene stacks. According to the simulations, acetaminophen is more likely to be attracted by the O-terminated carbon nanostructures grown on the HiDiPAN-1:12. The other configurations are also possible but with a much lower probability due to smaller adsorption energy. A summary of obtained results can be seen in Table 3.

According to the literature, the oxidation mechanism of paracetamol can be considered a one- or two- proton mechanism and it was extensively investigated in the literature. In the latter one, the electric system was exchanged with p–π conjugation (paracetamol) and π-π conjugation (product), resulting in a product having a lower energy level compared to the reactant [34]. Thus, the higher the presence of sp^2-bonded carbon atoms, as horizontally-aligned graphene sheets [39] or as vertically-aligned graphene stacks [34], the higher the formed π–π interaction with the product molecules. In our study, this aspect is well reflected by the electrode increasing sensitivity of acetaminophen with increasing sp^2-C content, as highlighted by the Raman spectroscopy results and by the acetaminophen oxidation peak shift for a higher CH_4:H_2 gas feed ratio. So, the reactant was easier to be oxidized, and the over-potential of paracetamol became lower than that on the bare H_2-treated composite with a shifting of 96 mV.

4. Conclusions

In this study, we prepared a metal-free carbon nanostructured fibrous electrode starting from PAN. We replaced the time-consuming carbonization phase with a single-step CVD process with a total duration of 40 minutes, in which we decorated the electrode surface with boron-doped carbon nanostructures, by simply varying the feed gas composition. The plasma has the function of shaping the fiber morphology, by etching the amorphous carbon on the fiber surface and growing a new carbon interface.

Acetaminophen detection sensitivity increases with the increasing CH_4:H_2 ratio during CVD nanostructure growth, while the linear interval range decreases. The best result, in terms of high sensitivity and low LOD, is represented by the vertically-aligned graphene stacks-decorated PAN composite. We attribute such improvement of the sensing performance to the MPECVD-grown nanoarchitecture. From a chemical perspective, the higher content of sp^2-C, jointly with the preferable presence of vacancy-like defects, favors the interaction with the analyte, resulting in an 18-fold increase of the sensitivity (compared to the fiber's turbostratic structure), while, from a physical and morphological perspective, the developed active surface and the existence of a purely diffusion-controlled process results in a low barrier to electron transfer, as shown by the lowest (92 mV) peak-to-peak separation. Moreover, molecular dynamics simulations support the hypothesis that the acetaminophen is preferably adsorbed on the top of the oxygen-terminated vertically-aligned graphene stacks, present in the HiDiPAN-1:12 composite.

Further studies are intended to investigate how to enhance the selectivity and sensitivity by tuning the defects and by heteroatom-doping, in order to develop rapid and inexpensive composite sensors.

CRediT authorship contribution statement

Mattia Pierpaoli: Conceptualization, Methodology, Formal analysis, Investigation, Data curation, Writing – original draft, Visualization, Project administration. **Pawel Jakóbczyk:** Methodology, Validation, Formal analysis, Investigation, Writing – original draft, Visualization. **Bartłomiej Dec:** Methodology, Software, Visualization. **Chiara Giosuè:** Data curation, Writing – review & editing. **Natalia Czerwińska:** Formal analysis, Writing – review & editing. **Aneta Lewkowicz:** Methodology, Formal analysis. **Maria Letizia Ruello:** Resources, Writing – review & editing. **Robert Bogdanowicz:** Resources, Writing – review & editing, Supervision, Project administration.

Table 3
Summary of adsorption energies and final distance of different NWs/acetaminophen configurations.

Configuration	E_{ads} (kcal/mol)	d (Å)
acetaminophen on side of CNW with O-termination	-12.94	3.25
acetaminophen on top of CNW with O-termination	-33	2.80
acetaminophen on top of CNW with H-termination	36.64	3.30

Declaration of Competing Interest

The authors declare that they have no known competing financial interests or personal relationships that could have appeared to influence the work reported in this paper.

Data Availability

Data will be made available on request.

Acknowledgments

This research was supported by the Polish National Agency for Academic Exchange (NAWA), under the Ulam program, Agreement No. PPN/ULM/2019/1/00061/DEC/1 (M. Pierpaoli), by the Argentum Triggering Research Grants (DEC-32/2020/IDUB/I.3.3) and from the STSM "Leaching behaviour of diamondized nanostructured sensors" supported by the COST Action CA 19118. Funding from Small grants program from the University of Gdansk (1220/29/2021- Aneta Lewkowicz) is also acknowledged.

Data availability

The project to realize the open-source wet-spinning apparatus is available online at the address: https://github.com/piermatt/wetspinnr. The raw data required to reproduce these findings can be provided upon email request to the corresponding author.

Supplementary materials

Supplementary material associated with this article can be found, in the online version, at doi:10.1016/j.electacta.2022.141083.

References

[1] S. Kim, Y.S. Chung, H.S. Choi, F.L. Jin, S.J. Park, Preparation and characterization of PAN-Based superfined carbon fibers for carbon-paper applications, Bull. Korean Chem. Soc. 34 (2013) 3733–3737, https://doi.org/10.5012/bkcs.2013.34.12.3733.
[2] W. Xu, B. Xin, X. Yang, Carbonization of electrospun polyacrylonitrile (PAN)/cellulose nanofibril (CNF) hybrid membranes and its mechanism, Cellulose 27 (2020) 3789–3804, https://doi.org/10.1007/s10570-020-03006-y.
[3] B. Saha, G.C. Schatz, Carbonization in polyacrylonitrile (PAN) based carbon fibers studied by ReaxFF molecular dynamics simulations, J. Phys. Chem. B 116 (2012) 4684–4692, https://doi.org/10.1021/jp300581b.
[4] N. Lu, C. Shao, X. Li, F. Miao, K. Wang, Y. Liu, CuO nanoparticles/nitrogen-doped carbon nanofibers modified glassy carbon electrodes for non-enzymatic glucose sensors with improved sensitivity, Ceram. Int. 42 (2016) 11285–11293, https://doi.org/10.1016/j.ceramint.2016.04.046.
[5] C. Guo, M. Hu, Z. Li, F. Duan, L. He, Z. Zhang, F. Marchetti, M. Du, Structural hybridization of bimetallic zeolitic imidazolate framework (ZIF) nanosheets and carbon nanofibers for efficiently sensing α-synuclein oligomers, Sens. Actuators B Chem. 309 (2020), 127821, https://doi.org/10.1016/j.snb.2020.127821.
[6] T. Yang, M. Du, H. Zhu, M. Zhang, M. Zou, Immobilization of Pt nanoparticles in carbon nanofibers: bifunctional catalyst for hydrogen evolution and electrochemical sensor, Electrochim. Acta 167 (2015) 48–54, https://doi.org/10.1016/j.electacta.2015.03.077.
[7] K. Mondal, M.A. Ali, C. Singh, G. Sumana, B.D. Malhotra, A. Sharma, Highly sensitive porous carbon and metal/carbon conducting nanofiber based enzymatic

biosensors for triglyceride detection, Sens. Actuators B Chem. 246 (2017) 202–214, https://doi.org/10.1016/j.snb.2017.02.050.
[8] P. Mohankumar, J. Ajayan, T. Mohanraj, R. Yasodharan, Recent developments in biosensors for healthcare and biomedical applications: a review, Meas. J. Int. Meas. Confed. 167 (2021), 108293, https://doi.org/10.1016/j.measurement.2020.108293.
[9] H. Zheng, Z. Yan, M. Wang, J. Chen, X. Zhang, Biosensor based on polyaniline-polyacrylonitrile-graphene hybrid assemblies for the determination of phenolic compounds in water samples, J. Hazard. Mater. 378 (2019), 120714, https://doi.org/10.1016/j.jhazmat.2019.05.107.
[10] O.C. Ozoemena, L.J. Shai, T. Maphumulo, K.I. Ozoemena, Electrochemical sensing of dopamine using onion-like carbons and their carbon nanofiber composites, Electrocatalysis 10 (2019) 381–391, https://doi.org/10.1007/s12678-019-00520-x.
[11] E.C. Almeida, M.R. Baldan, J.M. Rosolen, N.G. Ferreira, Impedance characteristics of the diamond/carbon fiber electrodes for electrical double-layer capacitor, Diam. Relat. Mater. 17 (2008) 1529–1533, https://doi.org/10.1016/j.diamond.2008.03.006.
[12] H.H. Zou, H. Bai, J.H. Yu, Y. Wang, Q.L. Liao, K. Nishimura, L.M. Zeng, N. Jiang, Architecting graphene nanowalls on diamond powder surface, Compos. Part B Eng. 73 (2015) 57–60, https://doi.org/10.1016/j.compositesb.2014.12.007.
[13] M. Pierpaoli, M. Ficek, P. Jakobczyk, J. Karczewski, R. Bogdanowicz, Self-assembly of vertically oriented graphene nanostructures: multivariate characterisation by Minkowski functionals and fractal geometry, Acta Mater. (2021), 116989, https://doi.org/10.1016/j.actamat.2021.116989.
[14] M. Pierpaoli, M. Ficek, M. Rycewicz, M. Sawczak, J. Karczewski, M. Ruello, R. Bogdanowicz, Tailoring electro/optical properties of transparent boron-doped carbon nanowalls grown on quartz, Materials 12 (2019) 547, https://doi.org/10.3390/ma12030547 (Basel).
[15] J. Li, S. Su, L. Zhou, V. Kundrát, A.M. Abbot, F. Mushtaq, D. Ouyang, D. James, D. Roberts, H. Ye, Carbon nanowalls grown by microwave plasma enhanced chemical vapor deposition during the carbonization of polyacrylonitrile fibers, J. Appl. Phys. (2013) 113, https://doi.org/10.1063/1.4774218.
[16] H.C. Hsu, C.H. Wang, S.K. Nataraj, H.C. Huang, H.Y. Du, S.T. Chang, L.C. Chen, K. H. Chen, Stand-up structure of graphene-like carbon nanowalls on CNT directly grown on polyacrylonitrile-based carbon fiber paper as supercapacitor, Diam. Relat. Mater. 25 (2012) 176–179, https://doi.org/10.1016/j.diamond.2012.02.020.
[17] Y. Chen, S. Zhang, H. Dai, Z. Hong, Y. Lin, A multiple mixed TiO_2 mesocrystal junction based PEC-colorimetric immunoassay for specific recognition of lipolysis stimulated lipoprotein receptor, Biosens. Bioelectron. 148 (2020), 111809.
[18] Y. Liu, Q. Sun, P. Yu, Y. Wu, L. Xu, H. Yang, M. Xie, T. Cheng, W.A. Goddard, Effects of high and low salt concentrations in electrolytes at lithium-metal anode surfaces using DFT-ReaxFF hybrid molecular dynamics method, J. Phys. Chem. Lett. 12 (2021) 2922–2929, https://doi.org/10.1021/acs.jpclett.1c00279.
[19] D.C. Liu, J. Nocedal, On the limited memory BFGS method for large scale optimization, Math. Program. 45 (1989) 503–528. https://link.springer.com/content/pdf/10.1007%2FBF01589116.pdf.
[20] H.J.C. Berendsen, J.P.M. Postma, W.F. Van Gunsteren, A. Dinola, J.R. Haak, Molecular dynamics with coupling to an external bath, J. Chem. Phys. 81 (1984) 3684–3690, https://doi.org/10.1063/1.448118.
[21] M.G. Dunham, D.D. Edie, Model of stabilization for pan-based carbon fiber precursor bundles, Carbon 30 (1992) 435–450. N. Y.
[22] A.K. Gupta, D.K. Paliwal, P. Bajaj, Acrylic precursors for carbon fibers, J. Macromol. Sci. Part C Polym. Rev. 31 (1991) 1–89.
[23] E. Cipriani, M. Zanetti, P. Bracco, V. Brunella, M.P. Luda, L. Costa, Crosslinking and carbonization processes in PAN films and nanofibers, Polym. Degrad. Stab. 123 (2016) 178–188, https://doi.org/10.1016/j.polymdegradstab.2015.11.008.
[24] A.C. Ferrari, S.E. Rodil, J. Robertson, S.E. Rodil, J. Robertson, Interpretation of infrared and Raman spectra of amorphous carbon nitrides, Phys. Rev. B Condens. Matter Mater. Phys. 67 (2003) 1–20, https://doi.org/10.1103/PhysRevB.67.155306.
[25] Z. Zafar, Z.H. Ni, X. Wu, Z.X. Shi, H.Y. Nan, J. Bai, L.T. Sun, Evolution of Raman spectra in nitrogen doped graphene, Carbon 61 (2013) 57–62, https://doi.org/10.1016/j.carbon.2013.04.065. N. Y.
[26] L.G. Cançado, A. Jorio, E.H.M. Ferreira, F. Stavale, C.A. Achete, R.B. Capaz, M.V. O. Moutinho, A. Lombardo, T.S. Kulmala, A.C. Ferrari, Quantifying defects in graphene via Raman spectroscopy at different excitation energies, Nano Lett. 11 (2011) 3190–3196, https://doi.org/10.1021/nl201432g.
[27] A.Y. Lee, K. Yang, N.D. Anh, C. Park, S.M. Lee, T.G. Lee, M.S. Jeong, Raman study of D* band in graphene oxide and its correlation with reduction, Appl. Surf. Sci. 536 (2021), 147990, https://doi.org/10.1016/j.apsusc.2020.147990.
[28] A. Sadezky, H. Muckenhuber, H. Grothe, R. Niessner, U. Pöschl, Raman microspectroscopy of soot and related carbonaceous materials: spectral analysis and structural information, Carbon 43 (2005) 1731–1742, https://doi.org/10.1016/j.carbon.2005.02.018. N. Y.
[29] D. López-Díaz, M. López Holgado, J.L. García-Fierro, M.M. Velázquez, Evolution of the Raman spectrum with the chemical composition of graphene oxide, J. Phys. Chem. C 121 (2017) 20489–20497, https://doi.org/10.1021/acs.jpcc.7b06236.
[30] D. Banerjee, K.J. Sankaran, S. Deshmukh, M. Ficek, G. Bhattacharya, J. Ryl, D. M. Phase, M. Gupta, R. Bogdanowicz, I.N. Lin, A. Kanjilal, K. Haenen, S.S. Roy, 3D hierarchical boron-doped diamond-multilayered graphene nanowalls as an efficient supercapacitor electrode, J. Phys. Chem. C (2019), https://doi.org/10.1021/acs.jpcc.9b03628.
[31] K.J. Sankaran, M. Ficek, S. Kunuku, K. Panda, C.J.J. Yeh, J.Y. Park, M. Sawczak, P. P. Michałowski, K.C.C. Leou, R. Bogdanowicz, I.N.N. Lin, K. Haenen, Self-organized multi-layered graphene-boron-doped diamond hybrid nanowalls for high-performance electron emission devices, Nanoscale 10 (2018) 1345–1355, https://doi.org/10.1039/c7nr06774g.
[32] K. Siuzdak, M. Ficek, M. Sobaszek, J. Ryl, M. Gnyba, P. Niedziałkowski, N. Malinowska, J. Karczewski, R. Bogdanowicz, Boron-enhanced growth of micron-scale carbon-based nanowalls: a route toward high rates of electrochemical biosensing, ACS Appl. Mater. Interfaces 9 (2017) 12982–12992, https://doi.org/10.1021/acsami.6b16860.
[33] A. Dettlaff, M. Sobaszek, T. Klimczuk, R. Bogdanowicz, Enhanced electrochemical kinetics of highly-oriented (111)-textured boron-doped diamond electrodes induced by deuterium plasma chemistry, Carbon 174 (2021) 594–604, https://doi.org/10.1016/j.carbon.2020.11.096. N. Y.
[34] P. Niedziałkowski, Z. Cebula, N. Malinowska, W. Białobrzeska, M. Sobaszek, M. Ficek, R. Bogdanowicz, J.S. Anand, T. Ossowski, Comparison of the paracetamol electrochemical determination using boron-doped diamond electrode and boron-doped carbon nanowalls, Biosens. Bioelectron. 126 (2019) 308–314, https://doi.org/10.1016/j.bios.2018.10.063.
[35] M. Pierpaoli, P. Jakobczyk, M. Sawczak, A. Łuczkiewicz, S. Fudala-Książek, R. Bogdanowicz, Carbon nanoarchitectures as high-performance electrodes for the electrochemical oxidation of landfill leachate, J. Hazard. Mater. 401 (2021), 123407, https://doi.org/10.1016/j.jhazmat.2020.123407.
[36] H. Li, K. Zhou, J. Cao, Q. Wei, C. Te Lin, S.E. Pei, L. Ma, N. Hu, Y. Guo, Z. Deng, Z. Yu, S. Zeng, W. Yang, L. Meng, A novel modification to boron-doped diamond electrode for enhanced, selective detection of dopamine in human serum, Carbon 171 (2021) 16–28, https://doi.org/10.1016/j.carbon.2020.08.019. N. Y.
[37] A. Dettlaff, P. Jakóbczyk, M. Ficek, B. Wilk, M. Szala, J. Wojtas, T. Ossowski, R. Bogdanowicz, Electrochemical determination of nitroaromatic explosives at boron-doped diamond/graphene nanowall electrodes: 2,4,6-trinitrotoluene and 2,4,6-trinitroanisole in liquid effluents, J. Hazard. Mater. 387 (2020), 121672, https://doi.org/10.1016/j.jhazmat.2019.121672.
[38] R. Zhang, C. Zhang, F. Zheng, X. Li, C.L. Sun, W. Chen, Nitrogen and sulfur co-doped graphene nanoribbons: a novel metal-free catalyst for high performance electrochemical detection of 2, 4, 6-trinitrotoluene (TNT), Carbon 126 (2018) 328–337, https://doi.org/10.1016/j.carbon.2017.10.042. N. Y.
[39] X. Kang, J. Wang, H. Wu, J. Liu, I.A. Aksay, Y. Lin, A graphene-based electrochemical sensor for sensitive detection of paracetamol, Talanta 81 (2010) 754–759, https://doi.org/10.1016/j.talanta.2010.01.009.
[40] S. Lotfi, H. Veisi, B. Karmakar, A convenient strategy for the electrochemical evaluation of acetaminophen and caffeine in combined drugs and biological samples over TiO2@polymethyldopa/Pd nanocomposite functionalized glassy carbon electrodes, Meas. J. Int. Meas. Confed. 186 (2021), 110156, https://doi.org/10.1016/j.measurement.2021.110156.
[41] M. Sobaszek, K. Siuzdak, J. Ryl, M. Sawczak, S. Gupta, S.B. Carrizosa, M. Ficek, B. Dec, K. Darowicki, R. Bogdanowicz, Diamond phase (sp3-C) rich boron-doped carbon nanowalls (sp2-C): physicochemical and electrochemical properties, J. Phys. Chem. C 121 (2017) 20821–20833, https://doi.org/10.1021/acs.jpcc.7b06365.
[42] L.A. Currie, Nomenclature in evaluation of analytical methods including detection and quantification capabilities (IUPAC recommendations 1995), Anal. Chim. Acta 391 (1999) 105–126, https://doi.org/10.1016/S0003-2670(99)00104-X.
[43] A. Eckmann, A. Felten, A. Mishchenko, L. Britnell, R. Krupke, K.S. Novoselov, C. Casiraghi, Probing the nature of defects in graphene by Raman spectroscopy, Nano Lett. 12 (2012) 3925–3930, https://doi.org/10.1021/nl300901a.
[44] E.H. Martins Ferreira, M.V.O. Moutinho, F. Stavale, M.M. Lucchese, R.B. Capaz, C. A. Achete, A. Jorio, Evolution of the Raman spectra from single-, few-, and many-layer graphene with increasing disorder, Phys. Rev. B Condens. Matter Mater. Phys. (2010) 82, https://doi.org/10.1103/PhysRevB.82.125429.
[45] E. Del Corro, M. Taravillo, V.G. Baonza, Stress-dependent correlations for resonant Raman bands in graphite with defects, J. Raman Spectrosc. 45 (2014) 476–480, https://doi.org/10.1002/jrs.4475.
[46] P. Mallet-Ladeira, P. Puech, C. Toulouse, M. Cazayous, N. Ratel-Ramond, P. Weisbecker, G.L. Vignoles, M. Monthioux, A Raman study to obtain crystallite size of carbon materials: a better alternative to the Tuinstra-Koenig law, Carbon 80 (2014) 629–639, https://doi.org/10.1016/j.carbon.2014.09.006. N. Y.
[47] M. Velický, P.S. Toth, C.R. Woods, K.S. Novoselov, R.A.W. Dryfe, Electrochemistry of the basal plane versus edge plane of graphite revisited, J. Phys. Chem. C 123 (2019) 11677–11685, https://doi.org/10.1021/acs.jpcc.9b01010.
[48] M. Doshi, E.P. Fahrenthold, Explosive molecule sensing at lattice defect sites in metallic carbon nanotubes, Mater. Adv. 2 (2021) 6315–6325, https://doi.org/10.1039/d1ma00571e.